

In-plane anisotropic charge dynamics in the layered polar Dirac semimetal BaMnSb₂H. Yoshizawa¹,[✉] H. Sakai²,[✉] M. Kondo,² M. Ochi³,[✉] K. Kuroki,² N. Hanasaki,² and J. Fujioka¹¹*Institute of Materials Science, University of Tsukuba, Ibaraki 305-8573, Japan*²*Department of Physics, Osaka University, Osaka 560-0043, Japan*³*Forefront Research Center, Osaka University, Osaka 560-0043, Japan*

(Received 20 April 2022; accepted 24 May 2022; published 15 June 2022)

We have studied the charge dynamics for the layered polar Dirac semimetal BaMnSb₂ by means of optical spectroscopy and *ab initio* calculation. A large anisotropy in the optical conductivity spectra is observed for two orthogonal light polarizations E^ω , both of which are perpendicular to the stacking direction of monoatomic layers; a clear peak emerges at the absorption edge of the Dirac band for E^ω parallel to the zigzag chain in the distorted Sb square net, but a tiny kink is observed for E^ω perpendicular to the chain. We also found that the effective electron mass is about an order of magnitude larger in the direction perpendicular to the chain than parallel to it. The theoretical calculation suggests that the dispersion of the Dirac band perpendicular to the chain is suppressed due to the reduced orbital hybridization, leading to the large in-plane electronic anisotropy.

DOI: [10.1103/PhysRevB.105.L241110](https://doi.org/10.1103/PhysRevB.105.L241110)

The quantum phenomena of relativistic electrons in Dirac/Weyl semimetals are issues of great interest in modern condensed-matter physics. A remarkable feature of Dirac/Weyl semimetals is that the electronic structure is intimately coupled to the crystal/magnetic structure, and its control often highlights salient features of relativistic electrons [1]. For example, in magnetic Weyl semimetals, the band crossing points (Weyl nodes) are coupled to the breakdown of time reversal symmetry due to the magnetic ordering or external magnetic field. Since the Weyl nodes act as the magnetic monopole/antimonopole in momentum space, one can induce the large anomalous Hall effect or magnetoresistance due to the chiral anomaly by tuning the nodal structure or band dispersion [2–10].

Another example is the spin-split gapped Dirac semimetal coupled to the breakdown of the spatial inversion symmetry. In this class of Dirac semimetal, the inversion asymmetry of the crystal structure causes the momentum-dependent spin splitting via the spin-orbit coupling (SOC) [11,12]. Recent studies demonstrated that such a Dirac semimetallic state emerges in the layered polar antiferromagnets BaMnX₂ (X=Bi, Sb), in which the multiple-valley structure of the spin-split Dirac band is varied by controlling the polar lattice distortion [13–15]. In particular, BaMnSb₂ is a semimetal with only the two valleys crossing the Fermi energy E_F . This material is a member of AMnX₂-type pnictides (A=Eu, Yb, alkali-earth ions) [15–29], and the crystal structure (with space group *Imm2*) can be viewed as the stacking of the Sb layer, Ba layer, and MnSb layer along the *b* axis, as illustrated in Fig. 1(a) [13,14]. As illustrated in Fig. 1(b), the Sb layer consists of the distorted square net with short and long Sb-Sb bonds, which can be viewed as a zigzag chain of Sb ions along the *a* axis. Due to the lack of mirror symmetry perpendicular to the *c* axis, the lattice polarization emerges along the *c* axis. We also note that the Mn 3*d* spins of the

MnSb layer antiferromagnetically order at $T_N = 285$ K while retaining the polar crystal structure. The theoretical calculation predicts that a spin-split Dirac band dispersion with a gap size of about 0.18 eV emerges near the *Y* point in momentum space [see Fig. 1(d)] [13,14]. In fact, a study on the transport measurement and angle-resolved photoemission spectroscopy revealed that there are two small hole pockets on the *Y-M* line due to the spin-split Dirac band [see Fig. 1(c)], which causes the bulk quantum Hall effect at low temperatures [13,14].

In general, the in-plane lattice asymmetry would cause not only the spin splitting but also the anisotropy of the electronic state, which has not been well understood so far in the present material. In this study, we explore the electronic state of BaMnSb₂ by means of optical spectroscopy and *ab initio* calculations on the basis of density functional theory. The optical conductivity spectra and loss function spectra show a significantly anisotropic interband transition and the Drude response of the Dirac electrons for the two orthogonal light polarizations, which are both perpendicular to the stacking direction of the monoatomic layer. In particular, the effective mass of the Dirac electron is about one order of magnitude larger in the direction perpendicular to the Sb zigzag chain than in the direction along the chain, which likely originates from the reduced orbital hybridization inherent in the orthorhombic crystal symmetry.

The single-crystalline samples of BaMnSb₂ were grown by the self-flux method [13]. The reflectivity spectra were measured in the geometry of nearly normal incidence with a typical beam spot of 0.2 mm in the energy region of 0.015–5 eV. Since the beam spot is smaller than the typical size of a single domain (~0.5 mm) [31], it is possible to measure the light polarization E^ω dependence of the reflectivity spectra. We used a Fourier transform spectrometer (grating-type monochromator) equipped with a microscope in the energy

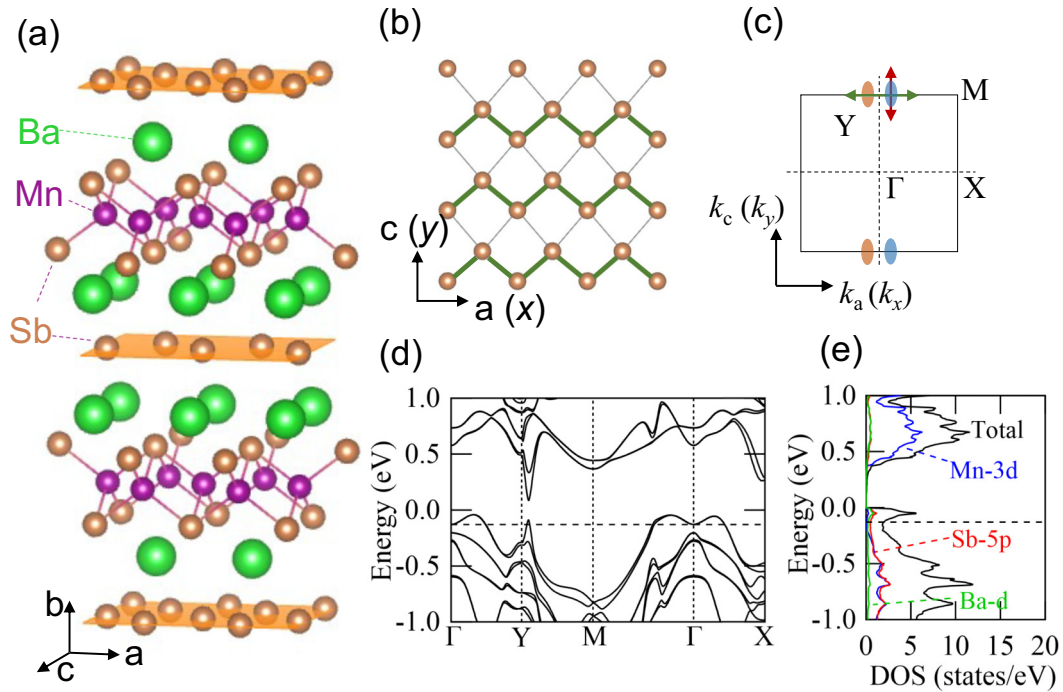


FIG. 1. (a) Illustration of the crystal structure of BaMnSb_2 drawn using VESTA [30]. (b) Illustration of the asymmetrically distorted square net of Sb. The green lines denote the shorter Sb-Sb bond, which highlights the Sb zigzag chain structure. The chain is along the a axis (x axis), and the perpendicular direction is the c axis (y axis). (c) Illustration of the first Brillouin zone on the Γ - X - Y plane. The light blue and red ellipsoids denote the hole pockets with S_z down-spin polarization and S_z up-spin polarization, respectively [see also Fig. 4(a)]. The arrows schematically show the k path of the electronic structure shown in Figs. 4(a) and 4(b). (d) The calculated electronic structure reproduced from Ref. [13] and (e) the partial density of states. The horizontal dashed line denotes E_F derived in Ref. [13].

region of 0.015–0.7 eV (0.5–5 eV). In the region of 4–30 eV, we carried out the measurement at room temperature using synchrotron radiation at UVSOR, Institute for Molecular Science (Okazaki). The optical conductivity spectrum and the loss function spectrum are derived by Kramers-Kronig analysis. For the analysis, we adopted the Hagen-Rubens-type extrapolation below 0.015 eV and ω^4 -type extrapolation above 30 eV. We performed first-principles calculations on the basis of the density functional theory with the Perdew-Burke-Ernzerhof parametrization of the generalized gradient approximation [32] and the projector augmented wave method [33] as implemented in the Vienna Ab initio Simulation Package (VASP) [34–37]. The spin-orbit coupling was included, and the G -type antiferromagnetic ordering of Mn 3d spin was assumed. First-principles calculations were performed using a body-centered tetragonal primitive cell. The experimental crystal structure determined at about 100 K was used [13].

Figures 2(a) and 2(b) show the reflectivity spectra for E^ω parallel to the chain ($E^\omega||a$) and those for E^ω perpendicular to the chain ($E^\omega||c$), respectively. The reflectivity spectra for $E^\omega||a$ show a high-reflectance band and plasma edge around 0.1 eV [see Fig. 2(a)]. Furthermore, several absorption peaks due to the interband transitions are observed in the energy region above 0.2 eV. With decreasing temperature, both the plasma edge and peaks of interband transition become pronounced and monotonically shift toward the higher-energy region. Similar high-reflectance band and absorption peaks are observed for $E^\omega||c$ [see Fig. 2(b)]. The energy of the plasma edge is slightly lower, and the absorption peaks of the

interband transitions are less pronounced compared with the case for $E^\omega||a$.

Figures 2(c) and 2(d) show the optical conductivity spectra $\sigma(\omega)$ for $E^\omega||a$ [$\sigma_a(\omega)$] and those for $E^\omega||c$ [$\sigma_c(\omega)$], respectively. At 300 K, the $\sigma_a(\omega)$ spectrum shows a steplike absorption edge at about 0.25 eV and a broad peak around 0.8 eV. With decreasing temperature, the steplike absorption edge shifts to the higher-energy region and gradually turns into a peak structure. The broad peak around 0.8 eV also slightly shifts to the higher-energy region and becomes more pronounced at lower temperatures. As shown in the inset in Fig. 2(c), the tail of the Drude peak is observed below 0.08 eV at 300 K but is gradually suppressed at lower temperatures. On the other hand, $\sigma_c(\omega)$ spectra show a more moderate temperature dependence; the absorption edge shows up as a small kink around 0.25 eV at 300 K, which shifts up to around 0.4 eV at 10 K without turning into a pronounced peak structure. The broad peak around 0.8 eV also shows a less pronounced temperature dependence. Note that the absorption edge shows the different spectral shapes between the $\sigma_a(\omega)$ spectra and the $\sigma_c(\omega)$ spectra, which likely originate from the anisotropy in the matrix element of the electric dipole transition [38–41], but the energies are nearly identical. From the viewpoint of the energy scale, it is reasonable to consider that the absorption edge corresponds to the threshold of the interband transition of spin-split Dirac electrons near the Y point [see Fig. 1(d)]. Indeed, it is known that (quasi-)two-dimensional Dirac semimetals or Dirac nodal line semimetals often show the steplike interband transition observed for

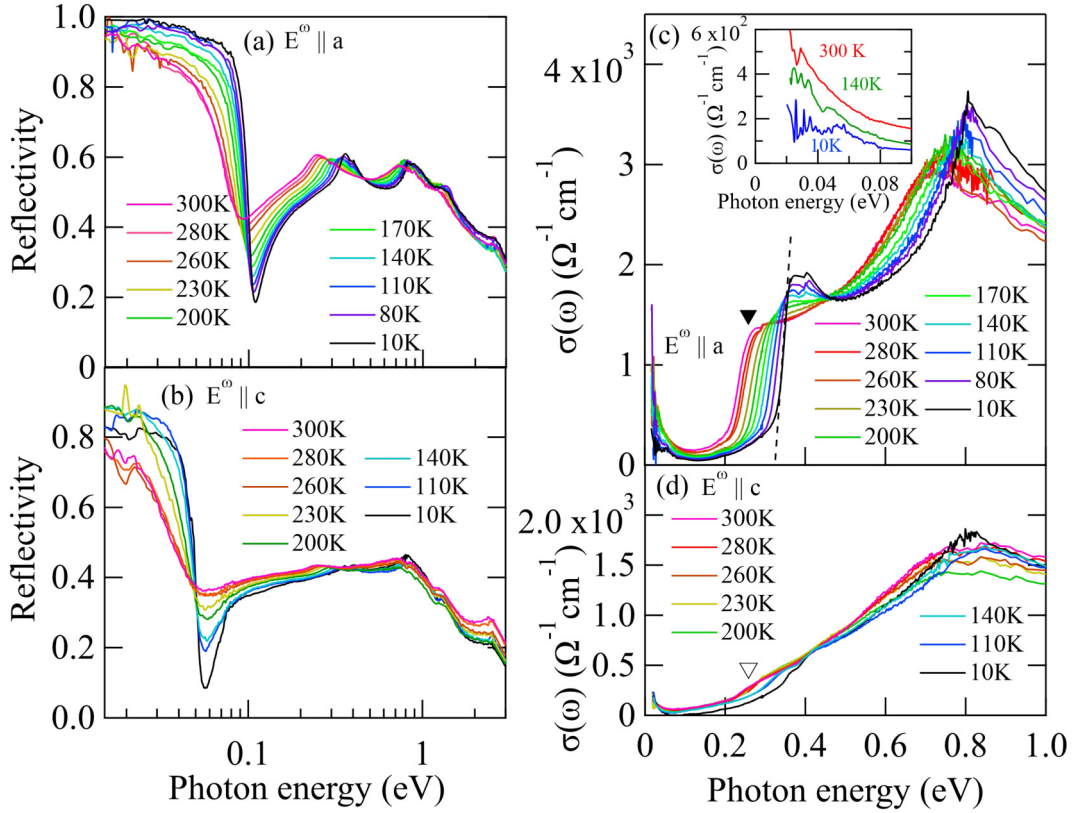


FIG. 2. Reflectivity spectra measured (a) for $E^\omega \parallel a$ and (b) for $E^\omega \parallel c$. Optical conductivity $\sigma(\omega)$ spectra (c) for $E^\omega \parallel a$ and (d) for $E^\omega \parallel c$. The inset in (c) shows a magnified view of $\sigma(\omega)$ spectra in the low-energy region. The solid and open triangles denote the absorption edge of the interband transition. The dashed line in (c) is an extrapolation to estimate the threshold energy of interband transition at 10 K.

$\sigma_a(\omega)$ spectra [42,43]. On the other hand, the broad peak around 0.8 eV seemingly includes the interband transition in other bands such as the bands near the Γ point. An interband transition with a similar threshold energy is also observed for $AMnSb_2$, with $A=Sr$ and Ca , which possesses an inversion symmetric crystal structure different from that of the present material [44,45].

We quantitatively estimate the threshold energy of the interband transition of the Dirac electron E_{th} by extrapolating the steeply rising part of the $\sigma(\omega)$ spectra with the ω -linear function as exemplified by the dashed line in Fig. 2(c). Here, we determine E_{th} on the basis of $\sigma_a(\omega)$ spectra since the accuracy was better than that derived from $\sigma_c(\omega)$ spectra. As shown in Fig. 3(a), with decreasing temperature from 300 to 10 K, E_{th} increases from 0.2 to more than 0.3 eV. To quantify the variation of the spectral shape near E_{th} , we also calculate the spectral intensity, i.e., the effective number of electrons, using the following formula:

$$N_{\text{eff}}^{\text{th}} = \frac{2m_0}{\pi e^2 N} \int_{E_{th}}^{E_{th}+0.2\text{eV}} \sigma(\omega) d\omega. \quad (1)$$

Here, m_0 and N are the free-electron mass and number of unit formula per unit volume, respectively. As shown in Fig. 3(b), $N_{\text{eff}}^{\text{th}}$ for the $\sigma_a(\omega)$ spectra is more than 3 times larger than that for the $\sigma_c(\omega)$ spectra at all temperatures. Note that both $N_{\text{eff}}^{\text{th}}$ for $E^\omega \parallel a$ and that for $E^\omega \parallel c$ substantially increase below T_N . This suggests that the antiferromagnetic ordering of the Mn

$3d$ state significantly changes the electronic state, as seen in the appearance of the peak structure at the absorption edge for $E^\omega \parallel a$. Indeed, the *ab initio* calculation shows that the Mn $3d$ state has a sizable weight, especially in the unoccupied state [see Fig. 1(e)]. Considering that the spectral shape changes on an energy scale of 1 eV, the electron correlation effect of the Mn $3d$ state may play an important role for the reconstruction of the electronic state as in the case of EuMnBi_2 [46].

The signature of the anisotropic electronic state is also seen in the Drude response. Since the majority of the Drude peak seems to be below the lower limit of measured energy, the fitting of $\sigma(\omega)$ spectra does not provide an accurate estimate of the Drude weight [see the inset in Fig. 2(c)]. Therefore, we estimate the Drude weight from the plasma frequency ω_p by using the optical sum rule that the Drude weight is scaled to $\omega_p^2/8$ [47]. In general, the imaginary part of the loss function $\text{Im}[-1/\epsilon(\omega)]$ shows a peak at the renormalized plasma frequency $\omega_p^* (= \omega_p/\sqrt{\epsilon_\infty})$, where ϵ_∞ is the dielectric constant arising from the optical excitation in the higher-energy region such as the interband transition. Thus, given that ϵ_∞ was determined from the spectra of the dielectric constant, we can estimate ω_p as well as the Drude weight by using the optical sum rule. As shown in Fig. 3(d), the $\text{Im}[-1/\epsilon(\omega)]$ spectra show peaks of plasma resonance around 0.08 and 0.04 eV for $E^\omega \parallel a$ and $E^\omega \parallel c$ at 300 K, respectively. With decreasing temperature, the peak for $E^\omega \parallel a$ shifts toward the higher-energy region, but the peak energy for $E^\omega \parallel c$ does not seem to significantly change. To quantitatively determine ω_p^* ,

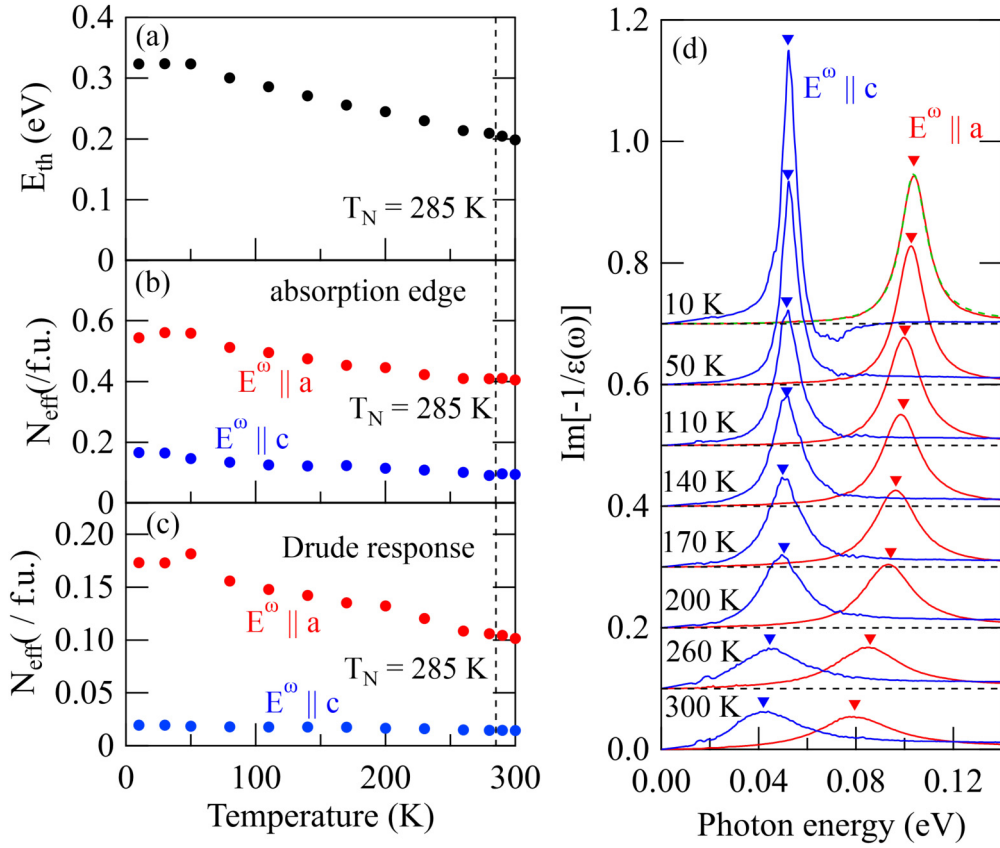


FIG. 3. (a) The threshold energy E_{th} of the interband transition of the Dirac band. (b) Spectral intensity of the interband transition near E_{th} . (c) Spectral intensity of the Drude response. (d) Imaginary part of the loss function spectra $\text{Im}[-1/\epsilon(\omega)]$ for $E^\omega \parallel a$ (red) and for $E^\omega \parallel c$ (blue). Spectra are offset for clarity. Triangles denote the peak of the plasma resonance. The dashed green curve exemplifies the fitting result performed for the spectrum at 10 K ($E^\omega \parallel a$).

we fitted $\text{Im}[-1/\epsilon(\omega)]$ spectra with the following classical oscillator model:

$$\text{Im}\left[-\frac{1}{\epsilon(\omega)}\right] = \frac{1}{\epsilon_\infty} \frac{\omega\gamma S_{\text{osc}}}{(\omega_p^{*2} - \omega^2)^2 + \omega^2\gamma^2}. \quad (2)$$

Here, γ and S_{osc} are the damping constant and oscillator strength of the plasma resonance, respectively. By using ϵ_∞ estimated from the real part of the dielectric function spectra [31], we calculated the Drude weight [see Fig. 3(c)]. The Drude weight for $E^\omega \parallel a$ significantly increases with decreasing temperature, whereas that for $E^\omega \parallel c$ does not significantly change. The former is about 9 times larger than the latter at 10 K, suggesting that the effective mass of the electron m^* is 9 times larger in the direction perpendicular to the chain than parallel to it. More specifically, given that the charge transport is nearly governed by Dirac electrons with a carrier density of about $9.3 \times 10^{18} \text{ cm}^{-3}$ [13], m^* is estimated to be $0.23m_0$ in the direction perpendicular to the chain and $0.026m_0$ along the chain.

To clarify the anisotropy of the Dirac band, we investigated the electronic structure near the Y point in momentum space using the *ab initio* calculation. Figure 4(a) shows the electronic structure on the Y - M line, i.e., in the direction parallel to the chain (k_a) [see also Fig. 1(c)]. For clarity, we define the Y point as the origin. Along k_a , the occupied state (unoccupied state) shows two maxima (minima) at $\pm 0.063\text{\AA}^{-1}$

with different spin polarizations. Near the top of the occupied state, the effective mass is estimated to be about $0.02m_0$. Figure 4(b) shows the electronic structure along k_c with fixed $k_a = 0.063\text{\AA}^{-1}$, i.e., on the line perpendicular to k_a , which passes through the maxima of the occupied state [see also Fig. 1(c)]. The dispersion along k_c is much more moderate than that along k_a . Consequently, m^* is estimated to be about $0.26m_0$, which is 13 times larger than that along k_a . The calculated m^* is nearly consistent with the experimental results, suggesting that the Drude response almost originates from the Dirac electron with anisotropic band dispersion, and the contribution from intraband transition at other bands, if any, is not significant. The band dispersion calculated without considering the SOC [see Figs. 4(a) and 4(b)] shows comparably large anisotropic behavior, suggesting that the spin splitting is not the direct origin of anisotropy.

Given that the band dispersion is quasi-two-dimensional and the carrier density is about $9.3 \times 10^{18} \text{ cm}^{-3}$ (determined from Ref. [13]), E_F is expected to be located about 0.07 eV (ΔE_F) below the maxima of the valence band. Assuming the electron-hole symmetric dispersion of the Dirac band with a gap of 0.18 eV (E_g), E_{th} is expected to be about 0.32 eV ($E_g + 2\Delta E_F$), which nearly agrees with the experimental result. In this sense, the sharp absorption peak near E_{th} observed for $\sigma_a(\omega)$ spectra may also originate from the large anisotropy of the band dispersion, which is reminiscent of the

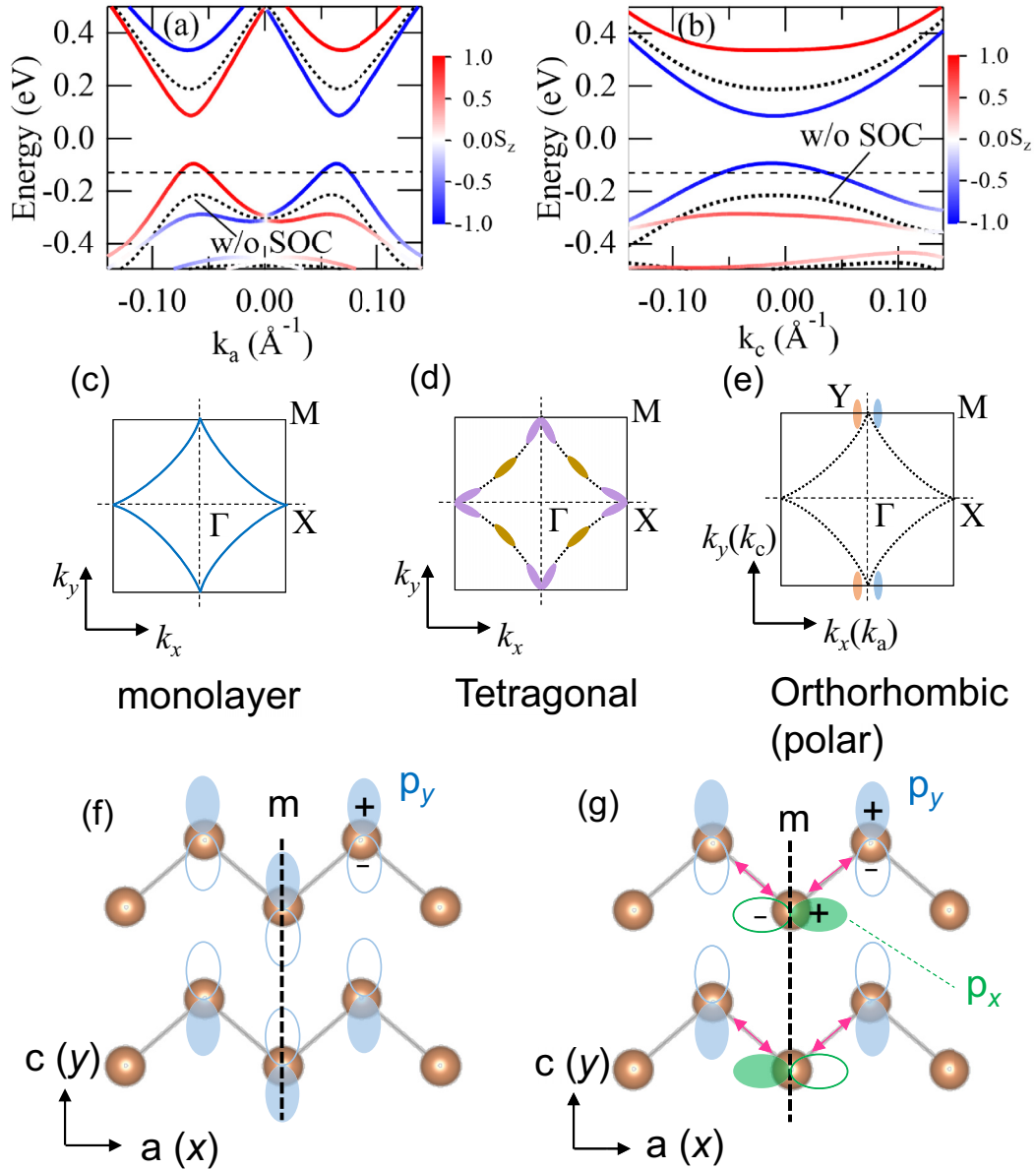


FIG. 4. The electronic structure (a) along k_a (Y - M line) and (b) along k_c with $k_a = 0.063 \text{ \AA}^{-1}$ [see also Fig. 1(c)] [31,48–50]. The color represents the z component of the spin polarization $\langle S_z \rangle$. The dotted curve denotes the calculated results without the spin-orbit coupling. The horizontal dashed line denotes E_F derived in Ref. [13]. Illustration of (c) the Dirac nodal line due to the tetragonal X square net on the $k_z = 0$ plane, (d) the calculated Fermi surface on the $k_z = 0$ plane while considering the interlayer interaction [16,19], and (e) the calculated Fermi surface on the $k_b = 0$ plane in BaMnSb_2 with orthorhombic crystal structure. Illustration of (f) the local $\text{Sb } 5p_y$ orbital and (g) the intersite $\text{Sb } 5p_x$ - $5p_y$ hybridization at the Y point. Vertical dashed lines denote the mirror plane (m) perpendicular to the chain. The intersite orbital hybridization is represented by the arrows on the right and left sides of the mirror plane, which interfere with each other.

sharp absorption edge in the quasi-one-dimensional electronic system.

The origin of the anisotropy of the Dirac band can be qualitatively understood by considering the electronic state originating from the Sb square net. In a series of AMnX_2 -type pnictides, it is proposed that the Dirac band mainly originates from the p state of the X square net [19,20]. According to Ref. [19], if both the SOC and the interlayer interaction between the X square net and A layer/ MX layer is negligible, the p state is expected to form the Dirac nodal line in the

vicinity of E_F , as shown in Fig. 4(c). In fact, the nodal line is gapped out by the interlayer interaction and the SOC, resulting in multiple valleys with an anisotropic shape of the Fermi surface, as exemplified in Fig. 4(d) [19]. It is argued that such an electronic state emerges in SrMnBi_2 with the tetragonal crystal structure [16]. In BaMnSb_2 , the orthorhombic lattice distortion further enhances the gap at some valleys, and consequently, the electron/hole pockets, except for two hole pockets near the Y point, vanish [see Fig. 4(e)] [13,14]. In other words, the anisotropic dispersion of the Dirac band

can be viewed as a remnant structure of the gapped Dirac line node. In this perspective, the larger (smaller) Drude response along k_a (k_c) can be attributed to the larger (smaller) band dispersion or conductivity perpendicular (parallel) to the gapped Dirac line node.

The anisotropic band dispersion near the Y point can be also explained in terms of the k -dependent orbital hybridization due to the crystal symmetry. The result of the *ab initio* calculation shows that the electronic state is mainly composed of the Sb $5p_y$ state at the Y point [$(k_a, k_c) = (0, \pi/c)$], as shown in Fig. 4(f). At the Y point, the intersite hybridization between Sb $5p_x$ - $5p_y$ orbitals is forbidden by the mirror symmetry perpendicular to the chain [see Fig. 4(g)]. This is a consequence of quantum interference [51,52]. With increasing k_a away from the Y point, the Sb $5p_x$ state gradually hybridizes with the Sb $5p_y$ state because of the broken mirror symmetry with respect to the Bloch phase with a nonzero k_a , resulting in a sizable energy dispersion along k_a . On the contrary, the orbital state remains approximately Sb $5p_y$ even when k_c changes from the Y point. This is because the Sb $5p_x$ - $5p_y$ hybridization is suppressed due to the mirror symmetry perpendicular to the chain as long as $k_a \sim 0$. As a result, the energy dispersion along k_c is moderate near the Y point. In other words, it is likely that the k dependence of Sb $5p_x$ - $5p_y$ hybridization causes the anisotropic dispersion of the Dirac band in the present materials.

In conclusion, we have investigated the electronic state of the layered polar Dirac semimetal BaMnSb₂ with a distorted Sb square net by means of optical spectroscopy and *ab initio* calculations. When the light polarization is parallel to the zigzag chain of the Sb square net ($E^\omega || a$), the optical conductivity spectra show a steplike absorption edge of the interband transition of the Dirac electron, which gradually changes into a sharp peak in the antiferromagnetic ordered phase at low temperatures. On the contrary, the spectra for the light polarization perpendicular to the zigzag chain ($E^\omega || c$) show a small kink at the absorption edge at all temperatures. The effective mass of the Dirac electron (hole-type carrier) estimated from the Drude response is about one order larger perpendicular to the chain, suggesting a highly anisotropic dispersion of the Dirac band. The theoretical calculation suggests that the occupied state of the Dirac band is mainly composed of the Sb $5p_x$ and Sb $5p_y$ mixed state, and their hybridization is selectively suppressed in the direction perpendicular to the chain due to the crystal symmetry, resulting in the large in-plane anisotropy of the Dirac band in the present material.

This work was partly supported by Grants-In-Aid for Science Research (Grants No. 18H01171, No. 19H01851, No. 21K18813, and No. 22H01177) from MEXT, by the Nippon Sheet Glass Foundation for Materials Science and Engineering, Japan, and by the Asahi Glass Foundation.

-
- [1] N. P. Armitage, E. J. Mele, and A. Vishwanath, *Rev. Mod. Phys.* **90**, 015001 (2018).
- [2] N. Nagaosa, J. Sinova, S. Onoda, A. H. MacDonald, and N. P. Ong, *Rev. Mod. Phys.* **82**, 1539 (2010).
- [3] H. B. Nielsen and M. Ninomiya, *Phys. Lett. B* **130**, 389 (1983).
- [4] A. A. Zyuzin and A. A. Burkov, *Phys. Rev. B* **86**, 115133 (2012).
- [5] D. T. Son and B. Z. Spivak, *Phys. Rev. B* **88**, 104412 (2013).
- [6] J. Xiong, S. K. Kushwaha, T. Liang, J. W. Krizan, M. Hirschberger, W. Wang, R. J. Cava, and N. P. Ong, *Science* **350**, 413 (2015).
- [7] T. Suzuki, R. Chisnell, A. Devarakonda, Y.-T. Liu, W. Feng, D. Xiao, J. W. Lynn, and J. G. Checkelsky, *Nat. Phys.* **12**, 1119 (2016).
- [8] E. Liu, Y. Sun, N. Kumar, L. Muechler, A. Sun, L. Jiao, S.-Y. Yang, D. Liu, A. Liang, Q. Xu, J. Kroder, V. Süß, H. Borrmann, C. Shekhar, Z. Wang, C. Xi, W. Wang, W. Schnelle, S. Wirth, Y. Chen, S. T. B. Goennenwein, and C. Felser, *Nat. Phys.* **14**, 1125 (2018).
- [9] K. Ueda, T. Oh, B.-J. Yang, R. Kaneko, J. Fujioka, N. Nagaosa, and Y. Tokura, *Nat. Commun.* **8**, 15515 (2017).
- [10] N. Kiyohara, T. Tomita, and S. Nakatsuji, *Phys. Rev. Appl.* **5**, 064009 (2016).
- [11] D. Xiao, W. Yao, and Q. Niu, *Phys. Rev. Lett.* **99**, 236809 (2007).
- [12] W. Yao, D. Xiao, and Q. Niu, *Phys. Rev. B* **77**, 235406 (2008).
- [13] H. Sakai, H. Fujimura, S. Sakuragi, M. Ochi, R. Kurihara, A. Miyake, M. Tokunaga, T. Kojima, D. Hashizume, T. Muro, K. Kuroda, T. Kondo, T. Kida, M. Hagiwara, K. Kuroki, M. Kondo, K. Tsuruda, H. Murakawa, and N. Hanasaki, *Phys. Rev. B* **101**, 081104(R) (2020).
- [14] J. Y. Liu *et al.*, *Nat. Commun.* **12**, 4062 (2021).
- [15] M. Kondo, M. Ochi, T. Kojima, R. Kurihara, D. Sekine, M. Matsubara, A. Miyake, M. Tokunaga, K. Kuroki, H. Murakawa, N. Hanasaki, and H. Sakai, *Commun. Mater.* **2**, 49 (2021).
- [16] J. Park, G. Lee, F. Wolff-Fabris, Y. Y. Koh, M. J. Eom, Y. K. Kim, M. A. Farhan, Y. J. Jo, C. Kim, J. H. Shim, and J. S. Kim, *Phys. Rev. Lett.* **107**, 126402 (2011).
- [17] J. K. Wang, L. L. Zhao, Q. Yin, G. Kotliar, M. S. Kim, M. C. Aronson, and E. Morosan, *Phys. Rev. B* **84**, 064428 (2011).
- [18] K. Wang, D. Graf, L. Wang, H. Lei, S. W. Tozer, and C. Petrovic, *Phys. Rev. B* **85**, 041101(R) (2012).
- [19] G. Lee, M. A. Farhan, J. S. Kim, and J. H. Shim, *Phys. Rev. B* **87**, 245104 (2013).
- [20] S. Borisenko, D. Evtushinsky, Q. Gibson, A. Yaresko, K. Koepf, T. Kim, M. N. Ali, J. van den Brink, M. Hoesch, A. Fedorov, E. Haubold, Y. Kushnirenko, I. Soldatov, R. Schäfer, and R. J. Cava, *Nat. Commun.* **10**, 3424 (2019).
- [21] Y. Feng *et al.*, *Sci. Rep.* **4**, 5385 (2015).
- [22] A. F. May, M. A. McGuire, and B. C. Sales, *Phys. Rev. B* **90**, 075109 (2014).
- [23] H. Masuda, H. Sakai, M. Tokunaga, Y. Yamasaki, A. Miyake, J. Shiozaki, S. Nakamura, S. Awaji, A. Tsukazaki, H. Nakao, Y. Murakami, T. Arima, Y. Tokura, and S. Ishiwata, *Sci. Adv.* **2**, e1501117 (2016).
- [24] A. Zhang, C. Liu, C. Yi, G. Zhao, T.-L. Xia, J. Ji, Y. Shi, R. Yu, X. Wang, C. Chen, and Q. Zhang, *Nat. Commun.* **7**, 13833 (2016).
- [25] J. Liu, J. Hu, H. Cao, Y. Zhu, A. Chuang, D. Graf, D. J. Adams, S. M. A. Radmanesh, L. Spinu, I. Chiorescu, and Z. Mao, *Sci. Rep.* **6**, 30525 (2016).

- [26] S. L. Huang, J. Kim, W. A. Shelton, E. W. Plummer, and R. Y. Jin, *Proc. Natl. Acad. Sci. USA* **114**, 6256 (2017).
- [27] L. Li, K. Wang, D. Graf, L. Wang, A. Wang, and C. Petrovic, *Phys. Rev. B* **93**, 115141 (2016).
- [28] C. Yi, S. Yang, M. Yang, L. Wang, Y. Matsushita, S. Miao, Y. Jiao, J. Cheng, Y. Li, K. Yamaura, Y. Shi, and J. Luo, *Phys. Rev. B* **96**, 205103 (2017).
- [29] S. Huang, L. Xing, R. Chapai, R. Nepal, and R. Jin, *Phys. Rev. Materials* **4**, 065001 (2020).
- [30] K. Momma and F. Izumi, *J. Appl. Crystallogr.* **44**, 1272 (2011).
- [31] See Supplemental Material at <http://link.aps.org/supplemental/10.1103/PhysRevB.105.L241110> for the electronic structure calculation, an illustration of the sample, and the dielectric function spectra.
- [32] J. P. Perdew, K. Burke, and M. Ernzerhof, *Phys. Rev. Lett.* **77**, 3865 (1996).
- [33] G. Kresse and D. Joubert, *Phys. Rev. B* **59**, 1758 (1999).
- [34] G. Kresse and J. Hafner, *Phys. Rev. B* **47**, 558(R) (1993).
- [35] G. Kresse and J. Hafner, *Phys. Rev. B* **49**, 14251 (1994).
- [36] G. Kresse and J. Furthmüller, *Comput. Mater. Sci.* **6**, 15 (1996).
- [37] G. Kresse and J. Furthmüller, *Phys. Rev. B* **54**, 11169 (1996).
- [38] I. Kézsmárki, Y. Shimizu, G. Mihály, Y. Tokura, K. Kanoda, and G. Saito, *Phys. Rev. B* **74**, 201101(R) (2006).
- [39] I. Kézsmárki, G. Mihály, R. Gaál, N. Barisić, A. Akrap, H. Berger, L. Forró, C. C. Homes, and L. Mihály, *Phys. Rev. Lett.* **96**, 186402 (2006).
- [40] M. Nakajima, T. Liang, S. Ishida, Y. Tomioka, K. Kihou, C. H. Lee, A. Iyo, H. Eisaki, T. Kakeshita, T. Ito, and S. Uchida, *Proc. Natl. Acad. Sci. USA* **108**, 12238 (2011).
- [41] S. Saberi-Pouya, T. Vazifehshenas, T. Salavati-fard, and M. Farmanbar, and F. M. Peeters, *Phys. Rev. B* **96**, 075411 (2017).
- [42] Z. Q. Li, E. A. Henriksen, Z. Jiang, Z. Hao, M. C. Martin, P. Kim, H. L. Stormer, and D. N. Basov, *Nat. Phys.* **4**, 532 (2008).
- [43] Y. Shao, Z. Sun, Y. Wang, C. Xu, R. Sankar, A. J. Breindel, C. Cao, M. M. Fogler, A. J. Millis, F. Chou, Z. Li, T. Timusk, M. B. Maple, and D. N. Basov, *Proc. Natl. Acad. Sci. USA* **116**, 1168 (2019).
- [44] H. J. Park, L. J. Sandilands, J. S. You, H. S. Ji, C. H. Sohn, J. W. Han, S. J. Moon, K. W. Kim, J. H. Shim, J. S. Kim, and T. W. Noh, *Phys. Rev. B* **93**, 205122 (2016).
- [45] Z. Qiu, C. Le, Y. Dai, B. Xu, J. B. He, R. Yang, G. Chen, J. Hu, and X. Qiu, *Phys. Rev. B* **98**, 115151 (2018).
- [46] H. Nishiyama, H. Sakai, K. Nakagawa, N. Hanasaki, S. Ishiwata, H. Masuda, M. Ochi, K. Kuroki, S. Iguchi, T. Sasaki, Y. Ikemoto, T. Moriwaki, K. Ueda, Y. Tokura, and J. Fujioka, *Phys. Rev. B* **104**, 115111 (2021).
- [47] M. Dressel and G. Gruner, *Electrodynamics of Solids* (Cambridge University Press, Cambridge, 2001).
- [48] N. Marzari and D. Vanderbilt, *Phys. Rev. B* **56**, 12847 (1997).
- [49] I. Souza, N. Marzari, and D. Vanderbilt, *Phys. Rev. B* **65**, 035109 (2001).
- [50] G. Pizzi *et al.*, *J. Phys.: Condens. Matter* **32**, 165902 (2020).
- [51] R. Akashi, Y. Iida, K. Yamamoto, and K. Yoshizawa, *Phys. Rev. B* **95**, 245401 (2017).
- [52] M. Ochi, R. Akashi, and K. Kuroki, *J. Phys. Soc. Jpn.* **85**, 094705 (2016).